nature materials

ARTICLES

PUBLISHED ONLINE: 31 AUGUST 2014 | DOI: 10.1038/NMAT4080

Phase-engineered low-resistance contacts for ultrathin MoS_2 transistors

Rajesh Kappera[1], Damien Voiry[1], Sibel Ebru Yalcin[2], Brittany Branch[2], Gautam Gupta[2], Aditya D. Mohite[2]* and Manish Chhowalla[1]*

Ultrathin molybdenum disulphide (MoS_2) has emerged as an interesting layered semiconductor because of its finite energy bandgap and the absence of dangling bonds. However, metals deposited on the semiconducting 2H phase usually form high-resistance (0.7 kΩ μm–10 kΩ μm) contacts, leading to Schottky-limited transport. In this study, we demonstrate that the metallic 1T phase of MoS_2 can be locally induced on semiconducting 2H phase nanosheets, thus decreasing contact resistances to 200–300 Ω μm at zero gate bias. Field-effect transistors (FETs) with 1T phase electrodes fabricated and tested in air exhibit mobility values of ~50 $cm^2 V^{-1} s^{-1}$, subthreshold swing values below 100 mV per decade, on/off ratios of $>10^7$, drive currents approaching ~100 $\mu A \mu m^{-1}$, and excellent current saturation. The deposition of different metals has limited influence on the FET performance, suggesting that the 1T/2H interface controls carrier injection into the channel. An increased reproducibility of the electrical characteristics is also obtained with our strategy based on phase engineering of MoS_2.

The presence of a finite bandgap and excellent electrostatic gate coupling in ultrathin two-dimensional materials such as molybdenum disulphide (MoS_2) make them interesting for electronics based on the current complementary metal oxide semiconductor (CMOS) paradigm[1–10]. Field-effect transistors (FETs) based on ultrathin MoS_2 channels have been widely studied because they exhibit large on/off ratios and near-theoretical subthreshold swing values[1,11–14]. Efforts towards further optimization of devices through fundamental understanding have led to studies investigating the influence of contact electrodes, intrinsic limitations in transport of carriers, and techniques for improving the mobility of MoS_2 devices[15–24]. Analysis of the literature reveals that mobility values, which are often used to demonstrate the quality of the material and devices, can vary from 1 to 400 $cm^2 V^{-1} s^{-1}$. The large deviation in mobility values arises from intrinsic challenges related to forming good contacts and differences in device fabrication and measurement procedures. For example, encapsulation of devices leads to substantial enhancement in mobility due to charge screening[1,15,25,26]. In the absence of encapsulation, removal of oxygen and water adsorbents via annealing[27–29], or measurement of properties in good vacuum[28,30–32] also result in increased mobility values. Multilayered samples in excess of ~5 layers typically show higher mobility than thinner materials[17,33].

Contact resistance is a key problem in ultrathin MoS_2 (1–10 layers) devices owing to the formation of a Schottky barrier for electron injection. Performance of MoS_2 FETs is strongly dependent on the metal used for source and drain electrodes[17,18,34]. In some studies, chemical interactions between the MoS_2 nanosheet and sulphide-forming metals such as Ti have been shown to detrimentally impact the device properties[10]. The most common electrode material used in MoS_2 FETs is gold, which in general yields reasonable device characteristics despite the large energy offset[1,35,36]. Detailed investigation of electrode materials with varying work functions has revealed that Fermi level pinning at the interface strongly impacts the device characteristics. Low-work-function metals with energy levels close to the conduction band of MoS_2 enhance the device performance[17] as a result of efficient injection of carriers, which in turn decreases the contact resistance.

For high-performance electronics, ideal contact electrodes consist of trap-free interfaces, possess low contact resistance, and are ohmic. In modern silicon-based microelectronics, this is achieved by designing source and drain contacts that are based on degenerately doped n++ or p++ regions on which metal pads are deposited. Thus the contact material is a highly conducting version of the channel material so that the interface resistance is low, structural mismatch is limited, and injection of carriers is facilitated. Similar strategies are used in III–V semiconductor technologies. Applying existing state-of-the-art schemes to improve contact properties in FETs from two-dimensional materials is not straightforward because their atomically thin nature makes doping challenging. Surface modification by molecules and ions can locally alter the conductivity[37], but such treatments suffer from long-term stability issues.

Here we demonstrate a new strategy based on phase engineering to design low-resistance contacts to realize FETs based on ultrathin MoS_2 with enhanced performance. We have developed a methodology to locally pattern the metallic 1T phase on ultrathin semiconducting MoS_2 nanosheets and use them as electrodes. We demonstrate contact resistances of 200–300 Ω μm at zero gate bias. The low contact resistance is attributed to the atomically sharp interface between the phases and to the fact the work function of the 1T phase and the conduction band energy relative to vacuum level of the 2H phase are similar (~4.2 eV). Both top- and bottom-gated devices with 1T electrodes show enhanced performance compared to devices in which metal is contacted directly to the semiconducting 2H phase. Specifically, we measure the properties in air and obtain mobility values of ~50 $cm^2 V^{-1} s^{-1}$, subthreshold swing values of 90–100 mV/decade, and on/off ratios of $>10^7$. Furthermore, device performance with 1T electrodes is

[1]Materials Science and Engineering, Rutgers University, 607 Taylor Road, Piscataway, New Jersey 08854, USA, [2]MPA-11 Materials Synthesis and Integrated Devices, Los Alamos National Laboratory, Los Alamos, New Mexico 87545, USA. *e-mail: amohite@lanl.gov; manish1@rci.rutgers.edu

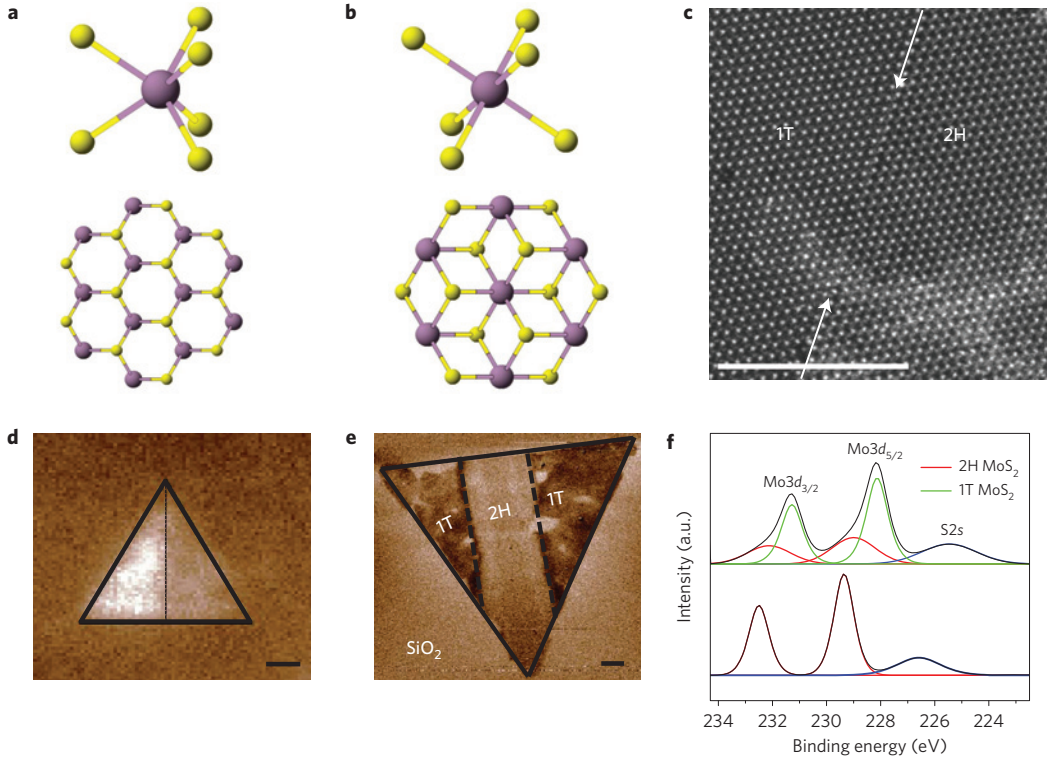

Figure 1 | 1T and 2H phases of MoS_2. a,**b**, Crystal structures of the 2H and 1T phases, respectively. In the upper diagram, trigonal prismatic (**a**) and octahedral (**b**) coordinations are shown. The lower panel shows the *c*-axis view of single-layer TMD with trigonal prismatic (**a**) and octahedral (**b**) coordinations. Atom colour code: purple, metal; yellow, chalcogen. **c**, High-resolution transmission electron microscope image of an atomically thin phase boundary (indicated by the arrows) between the 1T and 2H phases in a monolayered MoS_2 nanosheet. Scale bar, 1 nm. **d**, Photoluminescence map of a triangular monolayered MoS_2 nanosheet. The left side of the triangle is the 2H phase, whereas the right side was converted to the 1T phase. The 2H phase shows noticeably brighter PL than the 1T phase. **e**, Electrostatic force microscopy phase image of a monolayered MoS_2 nanosheet showing the difference between locally patterned 2H (bright colour) and 1T (dark colour) phases. Scale bars in **d**,**e** are 1 μm. **f**, XPS spectra showing the Mo3*d* and S2*s* peaks of the 1T and 2H phases of MoS_2. Typical experimentally measured spectra are shown in black and fits are shown in red (for the 2H phase component) and green (for the 1T phase component). The lower curve is 100% 2H phase, whereas the top curve can be fitted with both 1T and 2H phase components.

highly reproducible and independent of the type of contact metal pads used.

We have recently demonstrated the exfoliation of transition metal dichalcogenides (TMDs) such as MoS_2 and WS_2 (refs 38,39) using the well-known organolithium chemical method[40,41]. This synthesis route leads to the formation of the metallic 1T phase[38,42,43]. It has been shown that the 1T phase is stabilized by electron donation from the organolithium during intercalation[42,44–46]. As shown in previous studies by others[47–50], we have also demonstrated that the 1T phase is maintained even after complete removal of organolithium[38,39]. The 1T phase is metastable, with a relaxation energy of ∼1.0 eV for conversion to the thermodynamically stable 2H phase[39,51,52]. The crystal structures of the 2H and 1T phases are shown in Fig. 1a,b. High-resolution transmission electron microscopy has revealed that the 1T and 2H phases can coexist in the same TMD nanosheets and that the phase boundary between the two phases is atomically sharp with no visible defects, as shown in Fig. 1c (ref. 53). Local and patterned conversion of the semiconducting 2H phase to the metallic 1T phase is shown in Fig. 1d,e. The photoluminescence (PL) map of a chemical-vapour-deposited single-layer triangle of MoS_2 that has been partially converted to the 1T phase is shown in Fig. 1d. PL is substantially quenched in the region that has been converted to the 1T phase. The concentration of the 1T phase in the converted region was obtained by X-ray photoelectron spectroscopy (XPS) and found to be ∼60–70%, as shown in Fig. 1f (ref. 38). An electrostatic force microscopy (EFM) phase image of a micro-scale patterned 1T/2H/1T MoS_2 nanosheet is shown in Fig. 1e. The colour contrast in EFM arises from conducting and non-conducting regions on the single-layer nanosheet. The results in Fig. 1d,e indicate that local patterning of the 1T phase on 2H nanosheets is possible and the interface between the phases is sharp. The electronic properties of the 1T phase show that it is metallic, with an estimated carrier concentration of $>10^{13}$ cm^{-2}. The high electron density and metallic nature of the phase is also demonstrated by the fact that gate modulation in the 1T phase is absent, as shown in Fig. 3a.

All FET devices reported in this study were fabricated on mechanically exfoliated ultrathin nanosheets of MoS_2 (obtained from SPI) with thicknesses ranging from one to three layers on 100 nm of SiO_2/Si substrates. Source and drain electrodes were defined by lithographic patterning of the 1T phase, in which regions for conversion were left exposed while covering other regions with polymethylmethacrylate (PMMA). The uncovered regions were then treated with *n*-butyl lithium at room temperature for 1 h in a glove box (see Supplementary Information for details). The organic butyl residue and lithium ions were removed after treatment through thorough washing with hexane and de-ionized water, respectively[38]. The absence of lithium was confirmed by both electron energy-loss spectroscopy (EELS) in a scanning transmission electron microscope, as well as nuclear reaction analysis (NRA) shown in Supplementary Figs 9 and 10. Metal pads were then deposited on top of the 1T phase regions. After the 1T conversion, both top- and bottom-gated devices were processed (metal pad deposition and high *k* dielectric deposition) in exactly the same manner and simultaneously. Optical images of typical

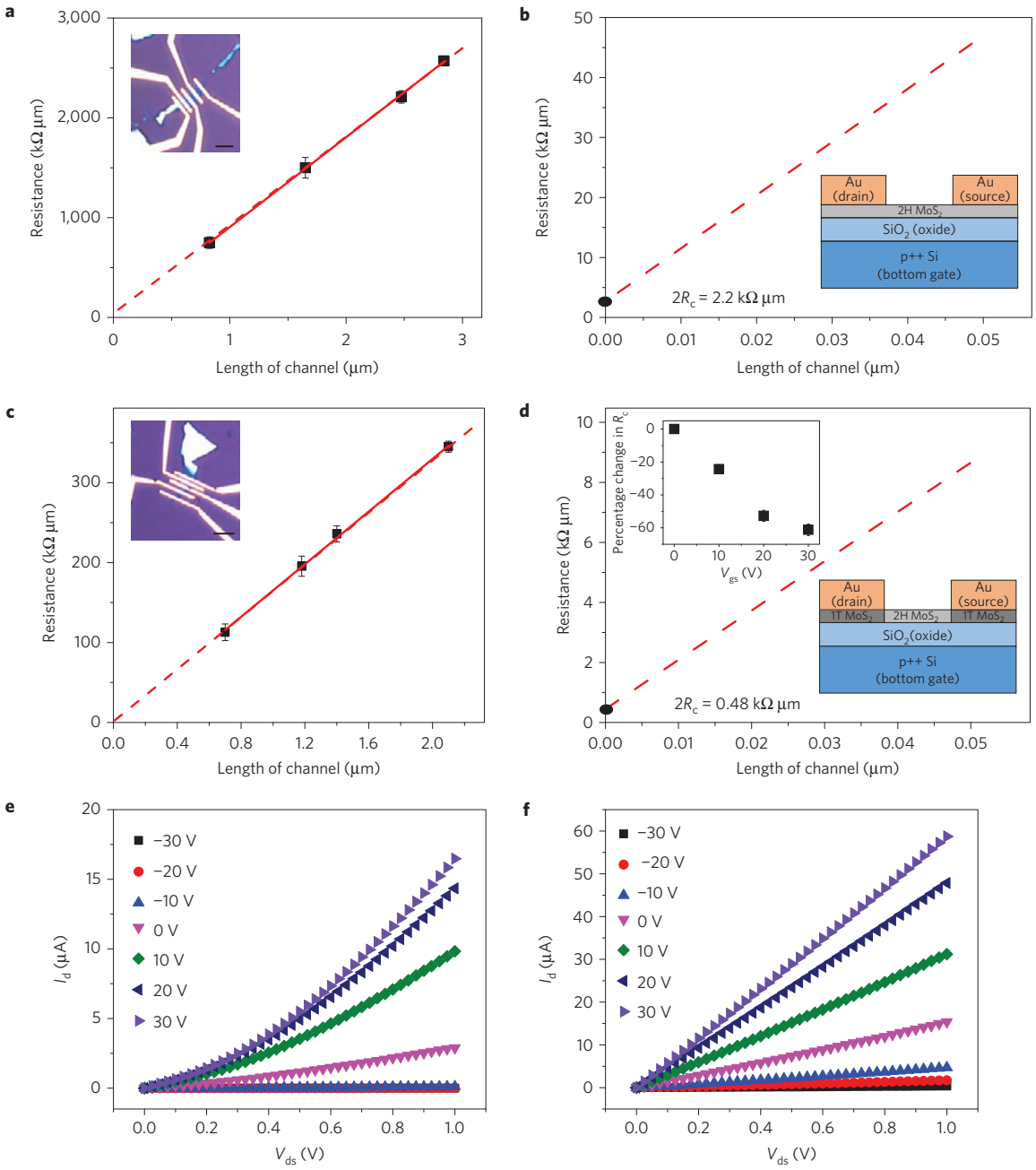

Figure 2 | Contact resistance of 1T and 2H phases. a–d, Resistance versus 2H channel lengths for Au deposited directly on the 2H phase (**a**,**b**) and on the 1T phase (**c**,**d**). Extrapolation of the red lines yields contact resistances (R_c) of 1.1 kΩ μm for 2H (**b**) and 0.2 kΩ μm for 1T (**d**) contacts at zero gate bias. Inset in **d** shows the percentage decrease in contact resistance with gate bias. Optical microscope images and device schematics are also shown. Scale bars in device photos are 5 μm. The channel in 1T electrode devices is shorter than in 2H devices owing to the diffusion of butyl lithium into the masked region. The error bars in **a**,**c** result from averaging of least five measurements on at least three devices. **e**,**f**, Drain current (I_d) characteristics of back-gated FETs for 0–1 V drain–source voltages (V_{ds}) and gate–source voltages V_{gs} ranging from −30 V to 30 V, showing Schottky behaviour for gold directly onto the 2H phase (**e**) and linear behaviour for the 1T electrodes (**f**).

devices are shown in Fig. 2. Top-gated devices were investigated through deposition of high *k* dielectrics by atomic layer deposition (ALD) or plasma-enhanced chemical vapour deposition (PECVD; see Supplementary Information for details).

The contact resistances were measured using the transfer length method (TLM), as shown in Fig. 2a–d. We tested two types of devices, shown schematically in Fig. 2b,d: ones in which the Au metal pads were contacted to the 1T phase and others in which the metal pads were contacted to the 2H phase directly. In both cases, the channel consisted of the 2H phase. To obtain good statistical analyses, at least 25 samples were measured and analysed. As with all electrical measurements reported in this work, the TLM resistances were measured in air and no annealing was performed. It can be seen from Fig. 2 that the resistance of the 1T contacts decreases by a factor of ~5 from 1.1 kΩ μm to 0.2 kΩ μm at zero gate bias. The 1T contact resistance values are lower than the best values of ~0.6–0.7 kΩ μm reported thus far for MoS_2 devices[5,7,8,54]. It also compares very favourably with the current state-of-the-art metal/silicon contacts in CMOS technology[55] (ITRS 2012 states source/drain parasitic resistance is in the range 0.3–0.5 kΩ μm (290 Ω μm, 405 Ω μm and

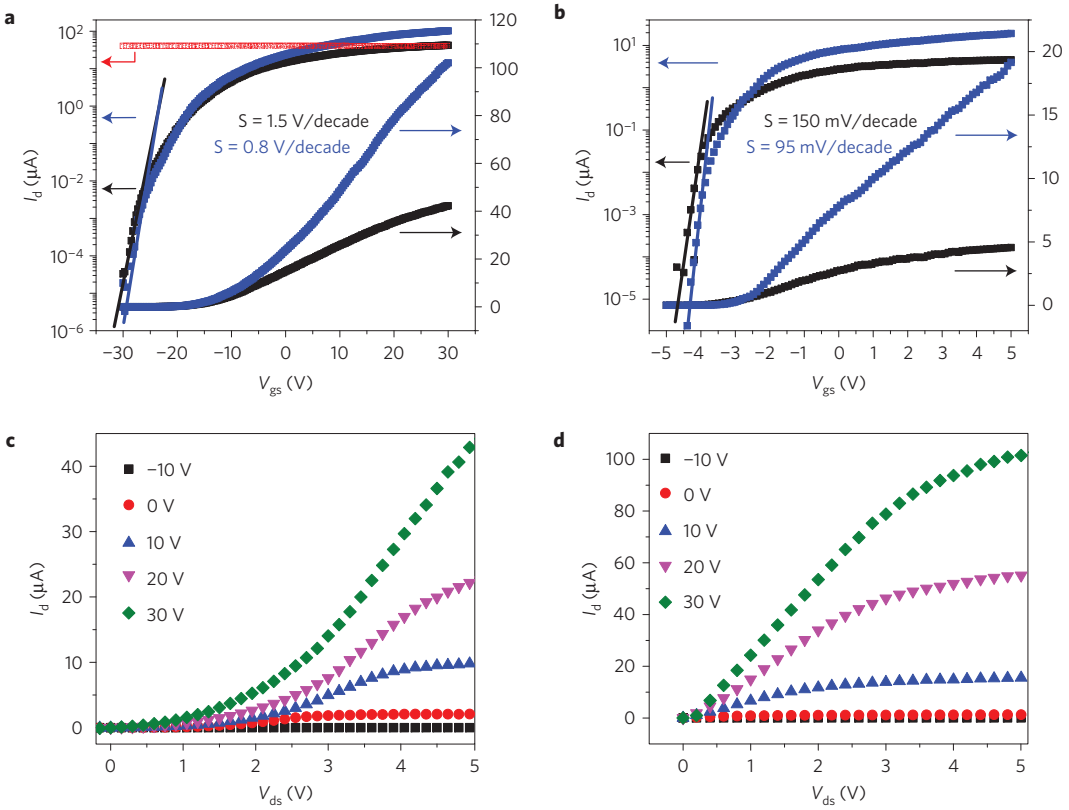

Figure 3 | Properties of field-effect transistors with 1T and 2H contacts. a,**b**, Transfer characteristics of bottom- and top-gated devices, respectively, measured at $V_{ds} = 1$ V. (Logarithmic scale on the left and linear scale on the right.) Blue curves represent devices with 1T phase electrodes and the black curves are with Au on the 2H phase. The red curve in **a** is the I_d 1T channel device, showing an absence of gate modulation owing to the metallic character of the 1T phase. The device width was 1.4 μm and device length was 1.2 μm. The linear fits used to extract the subthreshold swing values are also shown. **c**,**d**, Output characteristics of devices up to $V_{ds} = 5$ V and V_{gs} ranging from −10 V to 30 V, showing reasonable saturation for Au (**c**) and 1T electrodes (**d**).

467 Ω μm for planar, SOI and multigate low standby power CMOS, respectively), which is dominated by the contact resistance). We also found that the contact resistance decreases by another factor of three at a gate bias of +30 V, as shown in the inset of Fig. 2d. The improvement in device performance and reduction in contact resistance with 1T contacts is also highlighted in Fig. 2e,f. Clear nonlinear I_d–V_{ds} characteristics indicative of Schottky behaviour of metal pads directly on 2H contacts can be seen in Fig. 2e whereas ohmic-like behaviour (linear I_d–V_{ds}) is observed in Fig. 2f.

To translate the low contact resistances into device performance, we fabricated FETs with 1T phase source and drain electrodes and the 2H phase as the channel material. Both top- and bottom-gated devices were investigated and their properties measured in air. The 1T electrode devices always performed better in both configurations. The transfer characteristics of the bottom- and top-gated devices with and without 1T phase electrodes are shown in Fig. 3a,b. Large gate modulation of the channel can be seen, with on/off ratios of $>10^6$ in bottom-gated devices. It is immediately noticeable that the saturation currents with 1T phase electrodes are approximately three times higher than in devices with Au electrodes, which translates into slightly higher on/off ratios. The drive currents achieved in devices with 1T electrodes is 85 μA μm^{-1}, despite the MoS_2 channel being only 2–3 monolayers thick. In comparison, 30 μA μm^{-1} was achieved for devices with Au pads deposited directly on the 2H phase. As well as the very high drive currents, the transconductance value increased from ∼110 μA V^{-1} to 502 μA V^{-1} in the 1T phase electrode devices. These FET properties measured in air and without any encapsulation layer manifest into enhanced field-effect mobility values of ∼50 cm^2 V^{-1} s^{-1} for the 1T phase electrode devices compared to ∼15–20 cm^2 V^{-1} s^{-1} for the 2H contacts. The mobility values reported here can be further improved by elimination of any organic residues that might be present on the surface of MoS_2 as well as optimization of dielectric deposition and annealing procedures. The bottom-gate device characteristics are summarized in Table 1.

Table 1 | Comparison of bottom-gated devices.

Property	2H phase contacts	1T phase contacts	Ratio
On currents (μA μm^{-1})	30	85	2.8
Transconductance (μS μm^{-1})	1.4	3.8	2.7
Mobility (cm^2 V^{-1} s^{-1})	19	46	2.5
On/off ratio	10^7	10^8	10
Subthreshold swing (V/decade)	1.5	0.8	0.5

Top-gated devices were also fabricated and tested with 1T electrodes. We investigated a variety of gate dielectrics (HfO_2, SiO_2, Al_2O_3 and Si_3N_4) on top of ultrathin MoS_2 nanosheets. We first attempted to deposit HfO_2 using ALD and obtained reasonably good quality devices (see Supplementary Information for details). However, we found that the use of Si_3N_4 produced by PECVD as the gate dielectric also yielded highly reproducible, high-performance devices. Transfer characteristics of top-gated devices with and without 1T phase electrodes are shown in Fig. 3b. As with the back-gated devices, 1T electrodes enhance the performance of top-gated devices. In particular, excellent current saturation can be seen and the subthreshold swing values for the top-gated devices

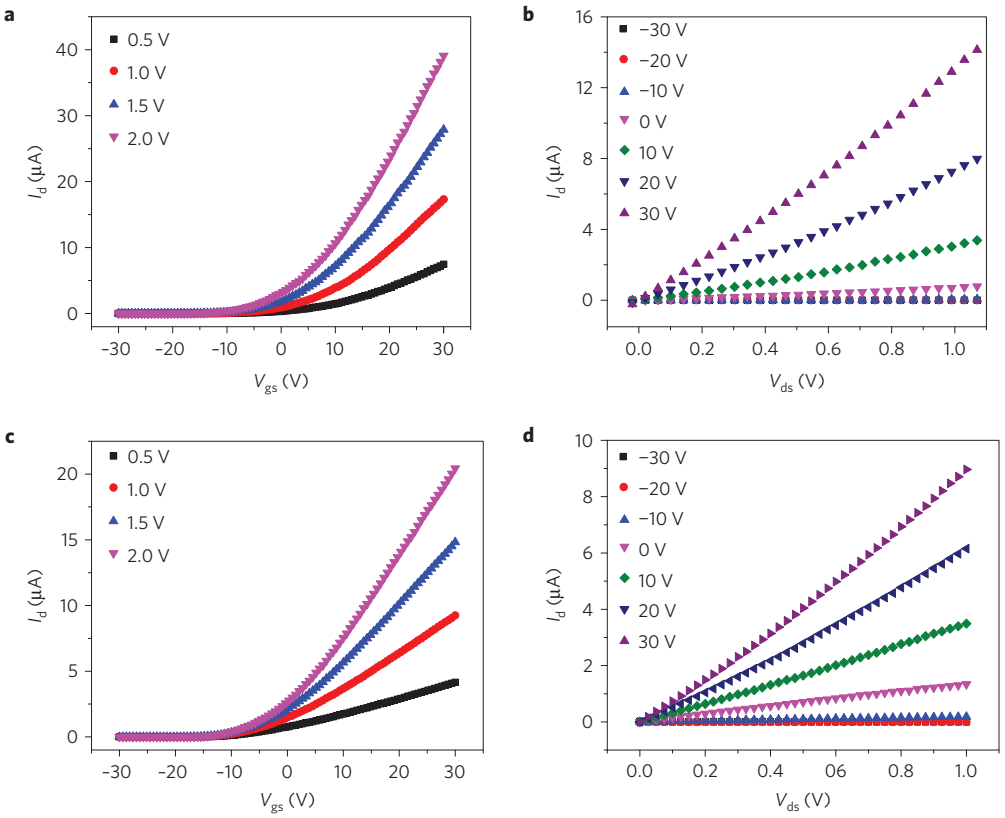

Figure 4 | Influence of the metal electrode work function on FET properties. a,**b**, Transfer (with V_{ds} ranging from 0.5 V to 2.0 V) and output (with V_{gs} ranging from −30 V to 30 V) characteristics, respectively, for devices with Pd deposited on top of 1T electrodes. **c**,**d**, Transfer and output characteristics, respectively, for devices with Ca deposited on top of 1T electrodes. The device properties are not substantially influenced by the work function of the metals used.

with 1T electrodes were found to be consistently in the range 90–100 mV/decade. In contrast, devices with Au directly on the 2H phase MoS_2 were found to be approximately 150 mV/decade. The differences in subthreshold swing between the two types of devices may be surprising since it depends on the channel capacitance, the capacitance of the dielectric, and capacitance from interface charges. All of these are expected to be similar in both devices. One reason for the lower subthreshold swing values in 1T devices could be the lower interface trap density, since the interface between the 1T and 2H phase is atomically sharp and the carrier density in the 1T phase is large. Another reason is that the actual channel length in the 1T phase devices is lower than the assumed value. This is because we have found that the butyl lithium diffuses into the channel under the PMMA so that some portion of the channel in the masked region is also converted to the 1T phase. As well as the shorter channel length, another advantage of the 1T electrodes could be that the source and drain electrodes are side contacts rather than vertical contacts. It has been discussed that side contacts could lead to better device properties in TMDs (refs 5,25). The saturation currents were also substantially larger in the 1T electrode devices (16 μA μm^{-1}) compared to 3 μA μm^{-1} on the non-phase-engineered electrodes. The lower drive currents in top-gated devices compared to back-gated devices is expected owing to underlap between gate electrode and source/drain. The absence of overlap means minimal barrier modulation and thus lower charge injection. The on/off ratio of both devices was found to be $>10^7$. Mobility values for top-gated devices have been shown to be substantially lower than back-gated devices[54]. We obtain values of ∼12–15 cm^2 V^{-1} s^{-1} for 1T metallic electrodes compared to 3–5 cm^2 V^{-1} s^{-1} for Au on 2H electrodes. The top-gate device characteristics are summarized in Table 2.

Table 2 | Comparison of top-gated devices.

Property	2H phase contacts	1T phase contacts	Ratio
On currents (μA μm^{-1})	3	16	5.3
Transconductance (μS μm^{-1})	1.1	3.1	2.8
Mobility (cm^2 V^{-1} s^{-1})	3.5	12.5	3.7
On/off ratio	10^6	10^7	10
Subthreshold swing (mV/decade)	150	95	0.6

To demonstrate that the true contact in the FET devices is between the 1T phase electrodes and the 2H phase channel, we investigated metal pads of varying work functions. As well as the Au metal pads used in the measurements reported thus far, we also tested calcium and palladium—low- and high-work-function metals. We found that reproducible FETs were challenging to fabricate when source/drain electrodes from these metals were directly deposited on to the 2H phase. For the working devices, the properties with Pd and Ca electrodes were relatively poor (see Supplementary Information for details) when deposited directly onto the 2H phase. In contrast, we found that highly reproducible devices with consistent properties in terms of mobility (20–30 cm^2 V^{-1} s^{-1}), saturation currents (30 μA μm^{-1}) and on/off ($>10^7$) ratio can be produced when metal pads are deposited on phase-engineered 1T electrodes. The FET transfer and output characteristics of back-gated devices with Ca and Pd metal pads deposited on the 1T phase are shown in Fig. 4. The fact that both devices perform reasonably similarly at room temperature despite the large differences in the metal work functions suggests that the

barrier for charge injection into the channel is at the 1T/2H interface and not at the metal/1T interface.

It is also worth noting that devices fabricated with 1T phase electrodes are highly reproducible and independent of the type of electrode metal used. In this study, we have fabricated and tested hundreds of devices with 1T electrodes; the yield of these devices is nearly 100% with consistent performance. In contrast, the yield of working devices fabricated with metals on top of the 2H phase was substantially lower and device characteristics were highly variable. The 1T phase is metastable, but we have demonstrated that it is stable under environmental conditions and also as catalyst for hydrogen evolution—however, its stability under high-performance device operation remains to be elucidated.

In summary, we have shown that phase engineering can markedly reduce the contact resistance between the source/drain electrodes and the channel to enable high-performance FETs. Specifically, we demonstrate that the metallic 1T phase is an effective contact electrode with record low-resistance values of 200 Ω μm at zero gate bias. The low contact resistance leads to unprecedentedly high drive currents (85 μA μm^{-1}), high mobility values, 95 mV/decade subthreshold swing values, and on/off ratios greater than 10^7. The excellent device properties we obtain are for a 1T phase concentration of ∼70%, suggesting that conversion to the pure 1T phase could lead to even greater enhancement in performance. Our work shows that phase engineering of electrodes is an effective strategy for further improving the performance of MoS_2 devices.

Methods

Local 1T phase transformation. After identifying the flakes on which the devices were to made, PMMA (C4 from Microchem) was spin-coated onto the sample at 3,000 r.p.m. for 60 s, followed by baking at 180 °C for 90 s. This was followed by e-beam lithography to remove PMMA from the portion(s) of the flake where 1T conversion was desired. To perform the phase transformation of the material, samples were immersed into 5 ml of 1.6 M *n*-butyl lithium (Sigma Aldrich) for two hours. All the butyl lithium exposure was done in a glove box in argon atmosphere at room temperature. Raman spectroscopy and XPS were used to confirm the phase transformation of MoS_2. The lithium was removed by thoroughly washing the samples.

Mobility extraction. The slope of the FET transfer characteristic in the linear region gives us the transconductance (g_m) of the device, which is the change in the drain–source current when the gate voltage is varied. This was substituted into the mobility formula obtained by taking a first-order derivative of the drain–source current equation in the linear mode of FET operation.

$$\mu = \frac{Lg_m}{WC_G V_{ds}}$$

where C_G is the back-gate capacitance. By inserting the appropriate values of the length (L) and width (W) of the device and the corresponding transconductance (g_m) at a particular V_{ds}, the mobility is obtained.

Received 21 April 2014; accepted 2 August 2014; published online 31 August 2014

References

1. Radisavljevic, B., Radenovic, A., Brivio, J., Giacometti, V. & Kis, A. Single-layer MoS_2 transistors. *Nature Nanotech.* **6,** 147–150 (2011).
2. Wang, Q. H., Kalantar-Zadeh, K., Kis, A., Coleman, J. N. & Strano, M. S. Electronics and optoelectronics of two-dimensional transition metal dichalcogenides. *Nature Nanotech.* **7,** 699–712 (2012).
3. Jariwala, D., Sangwan, V. K., Lauhon, L. J., Marks, T. J. & Hersam, M. C. Emerging device applications for semiconducting two-dimensional transition metal dichalcogenides. *ACS Nano* **8,** 1102–1120 (2014).
4. Zhu, W. *et al.* Electronic transport and device prospects of monolayer molybdenum disulphide grown by chemical vapour deposition. *Nature Commun.* **5,** 3087 (2014).
5. Das, S. & Appenzeller, J. Where does the current flow in two-dimensional layered systems? *Nano Lett.* **13,** 3396–3402 (2013).
6. Chang, H-Y., Zhu, W. & Akinwande, D. On the mobility and contact resistance evaluation for transistors based on MoS_2 or two-dimensional semiconducting atomic crystals. *Appl. Phys. Lett.* **104,** 113504 (2014).
7. Liu, H., Neal, A. T. & Ye, P. D. Channel length scaling of MoS_2 MOSFETs. *ACS Nano* **6,** 8563–8569 (2012).
8. Liu, H. *et al.* Switching mechanism in single-layer molybdenum disulfide transistors: An insight into current flow across Schottky barriers. *ACS Nano* **8,** 1031–1038 (2014).
9. Liu, W. *et al.* High-performance few-layer-MoS_2 field-effect-transistor with record low contact-resistance *Electron Devices Meet. IEDM 2013 IEEE Int.* 19.4.1–19.4.4 (2013).
10. McDonnell, S., Addou, R., Buie, C., Wallace, R. M. & Hinkle, C. L. Defect-dominated doping and contact resistance in MoS_2. *ACS Nano* **8,** 2880–2888 (2014).
11. Radisavljevic, B., Whitwick, M. B. & Kis, A. Integrated circuits and logic operations based on single-layer MoS_2. *ACS Nano* **5,** 9934–9938 (2011).
12. Wang, H. *et al.* Integrated circuits based on bilayer MoS_2 transistors. *Nano Lett.* **12,** 4674–4680 (2012).
13. Lee, H. S. *et al.* MoS_2 nanosheet phototransistors with thickness-modulated optical energy gap. *Nano Lett.* **12,** 3695–3700 (2012).
14. Yoon, Y., Ganapathi, K. & Salahuddin, S. How good can monolayer MoS_2 transistors be? *Nano Lett.* **11,** 3768–3773 (2011).
15. Jena, D. & Konar, A. Enhancement of carrier mobility in semiconductor nanostructures by dielectric engineering. *Phys. Rev. Lett.* **98,** 136805 (2007).
16. Walia, S. *et al.* Characterization of metal contacts for two-dimensional MoS_2 nanoflakes. *Appl. Phys. Lett.* **103,** 232105 (2013).
17. Das, S., Chen, H-Y., Penumatcha, A. V. & Appenzeller, J. High performance multilayer MoS_2 transistors with scandium contacts. *Nano Lett.* **13,** 100–105 (2013).
18. Chen, J-R. *et al.* Control of Schottky barriers in single layer MoS_2 transistors with ferromagnetic contacts. *Nano Lett.* **13,** 3106–3110 (2013).
19. Dankert, A., Langouche, L., Kamalakar, M. V. & Dash, S. P. High-performance molybdenum disulfide field-effect transistors with spin tunnel contacts. *ACS Nano* **8,** 476–482 (2014).
20. Chuang, S. *et al.* MoS_2 p-type transistors and diodes enabled by high work function MoO_x contacts. *Nano Lett.* **14,** 1337–1342 (2014).
21. Radisavljevic, B. & Kis, A. Mobility engineering and a metal–insulator transition in monolayer MoS_2. *Nature Mater.* **12,** 815–820 (2013).
22. Bao, W., Cai, X., Kim, D., Sridhara, K. & Fuhrer, M. S. High mobility ambipolar MoS_2 field-effect transistors: Substrate and dielectric effects. *Appl. Phys. Lett.* **102,** 042104 (2013).
23. Jariwala, D. *et al.* Band-like transport in high mobility unencapsulated single-layer MoS_2 transistors. *Appl. Phys. Lett.* **102,** 173107 (2013).
24. Lin, J. *et al.* Flexible metallic nanowires with self-adaptive contacts to semiconducting transition-metal dichalcogenide monolayers. *Nature Nanotech.* **9,** 436–442 (2014).
25. Kim, S. *et al.* High-mobility and low-power thin-film transistors based on multilayer MoS_2 crystals. *Nature Commun.* **3,** 1011 (2012).
26. Liu, H. & Ye, P. D. MoS_2 dual-gate MOSFET with atomic-layer-deposited Al_2O_3 as top-gate dielectric. *IEEE Electron Device Lett.* **33,** 546–548 (2012).
27. Baugher, B. W. H., Churchill, H. O. H., Yang, Y. & Jarillo-Herrero, P. Intrinsic electronic transport properties of high-quality monolayer and bilayer MoS_2. *Nano Lett.* **13,** 4212–4216 (2013).
28. Schmidt, H. *et al.* Transport properties of monolayer MoS_2 grown by chemical vapor deposition. *Nano Lett.* **14,** 1909–1913 (2014).
29. Sangwan, V. K. *et al.* Low-frequency electronic noise in single-layer MoS_2 transistors. *Nano Lett.* **13,** 4351–4355 (2013).
30. Qiu, H. *et al.* Electrical characterization of back-gated bi-layer MoS_2 field-effect transistors and the effect of ambient on their performances. *Appl. Phys. Lett.* **100,** 123104 (2012).
31. Park, W. *et al.* Oxygen environmental and passivation effects on molybdenum disulfide field effect transistors. *Nanotechnology* **24,** 095202 (2013).
32. Zhang, W. *et al.* High-gain phototransistors based on a CVD MoS_2 monolayer. *Adv. Mater.* **25,** 3456–3461 (2013).
33. Kang, J., Liu, W. & Banerjee, K. High-performance MoS_2 transistors with low-resistance molybdenum contacts. *Appl. Phys. Lett.* **104,** 093106 (2014).
34. Popov, I., Seifert, G. & Tománek, D. Designing electrical contacts to MoS_2 monolayers: A computational study. *Phys. Rev. Lett.* **108,** 156802 (2012).
35. Buscema, M. *et al.* Large and tunable photothermoelectric effect in single-layer MoS_2. *Nano Lett.* **13,** 358–363 (2013).
36. Ghatak, S., Pal, A. N. & Ghosh, A. Nature of electronic states in atomically thin MoS_2 field-effect transistors. *ACS Nano* **5,** 7707–7712 (2011).
37. Fang, H. *et al.* Degenerate n-doping of few-layer transition metal dichalcogenides by potassium. *Nano Lett.* **13,** 1991–1995 (2013).
38. Eda, G. *et al.* Photoluminescence from chemically exfoliated MoS_2. *Nano Lett.* **11,** 5111–5116 (2011).

39. Voiry, D. *et al.* Enhanced catalytic activity in strained chemically exfoliated WS_2 nanosheets for hydrogen evolution. *Nature Mater.* **12,** 850–855 (2013).
40. Dines, M. B. Lithium intercalation via n-butyl lithium of the layered transition metal dichalcogenides. *Mater. Res. Bull.* **10,** 287–291 (1975).
41. Joensen, P., Frindt, R. F. & Morrison, S. R. Single-layer MoS_2. *Mater. Res. Bull.* **21,** 457–461 (1986).
42. Py, M. A. & Haering, R. R. Structural destabilization induced by lithium intercalation in MoS_2 and related compounds. *Can. J. Phys.* **61,** 76–84 (1983).
43. Mulhern, P. J. Lithium intercalation in crystalline Li_xMoS_2. *Can. J. Phys.* **67,** 1049–1052 (1989).
44. Kertesz, M. & Hoffmann, R. Octahedral versus trigonal-prismatic coordination and clustering in transition-metal dichalcogenides. *J. Am. Chem. Soc.* **106,** 3453–3460 (1984).
45. Enyashin, A. N. & Seifert, G. Density-functional study of Li_xMoS_2 intercalates ($0 \leq x \leq 1$). *Comput. Theor. Chem.* **999,** 13–20 (2012).
46. Chhowalla, M. *et al.* The chemistry of two-dimensional layered transition metal dichalcogenide nanosheets. *Nature Chem.* **5,** 263–275 (2013).
47. Joensen, P., Crozier, E. D., Alberding, N. & Frindt, R. F. A study of single-layer and restacked MoS_2 by X-ray diffraction and X-ray absorption spectroscopy. *J. Phys. C* **20,** 4043–4053 (1987).
48. Jiménez Sandoval, S., Yang, D., Frindt, R. & Irwin, J. Raman study and lattice dynamics of single molecular layers of MoS_2. *Phys. Rev. B* **44,** 3955–3962 (1991).
49. Yang, D., Sandoval, S. J., Divigalpitiya, W. M. R., Irwin, J. C. & Frindt, R. F. Structure of single-molecular-layer MoS_2. *Phys. Rev. B* **43,** 12053–12056 (1991).
50. Heising, J. & Kanatzidis, M. G. Structure of restacked MoS_2 and WS_2 elucidated by electron crystallography. *J. Am. Chem. Soc.* **121,** 638–643 (1999).
51. Wypych, F. & Schollhorn, R. 1T-MoS_2, a new metallic modification of molybdenum disulfide. *J. Chem. Soc. Chem. Commun.* **19,** 1386–1388 (1992).
52. Tsai, H-L., Heising, J., Schindler, J. L., Kannewurf, C. R. & Kanatzidis, M. G. Exfoliated–restacked phase of WS_2. *Chem. Mater.* **9,** 879–882 (1997).
53. Eda, G. *et al.* Coherent atomic and electronic heterostructures of single-layer MoS_2. *ACS Nano* **6,** 7311–7317 (2012).
54. Fuhrer, M. S. & Hone, J. Measurement of mobility in dual-gated MoS_2 transistors. *Nature Nanotech.* **8,** 146–147 (2013).
55. *International Technology Roadmap for Semiconductors* www.itrs.net (ITRS, 2012).

Acknowledgements

M.C., R.K. and D.V. acknowledge financial support from NSF DGE 0903661 and NSF ECCS 1128335. R.K. acknowledges support and discussions with E. Garfunkel. We acknowledge T. Fujita for the EELS data and B. Yakshinskiy for NRA. This work was done in part at the Center for Integrated Nanotechnologies, an Office of Science User Facility.

Author contributions

M.C. conceived the idea, designed the experiments, analysed the data and wrote the manuscript. R.K., D.V. and A.D.M. conceived the idea and designed the experiments with M.C., synthesized the materials, fabricated the devices, made the measurements and analysed the data. S.E.Y. performed the AFM, EFM and PL mapping measurements. B.B. performed the gate dielectric depositions. G.G. helped to analyse the data and assisted in optimizing the 1T phase transformation chemistry. All the authors have read the manuscript and agree with its content.

Additional information

Supplementary information is available in the online version of the paper. Reprints and permissions information is available online at www.nature.com/reprints. Correspondence and requests for materials should be addressed to A.D.M. or M.C.

Competing financial interests

The authors declare no competing financial interests.